S_1-S_0 Internal Conversion in Ketene. 1. The Role of Conical Intersections

David R. Yarkony*

Department of Chemistry, The Johns Hopkins University, Baltimore, Maryland 21218

Received: March 24, 1999; In Final Form: June 8, 1999

The role of conical intersections in the internal conversion ($S_1 \rightarrow S_0$) of photoexcited ketene (H_2CCO) is analyzed. The energy-minimized projection of a portion of the $S_1(^1A'')-S_0(^1A')$ seam of the conical intersection near the minimum energy-crossing point is studied as a function of the key internal coordinates R(C−C) and ∠CCO. The characteristic parameters of the conical intersection points are used, to identify the two modes that evince the conical nature of the intersection, to determine the energy and singular part of the derivative coupling near the conical intersection, and to construct a transformation to diabatic states that rigorously removes the singularity in the derivative coupling. From the Franck−Condon region of the $S_0 \rightarrow S_1$ excitation, barrierless paths were identified on S_1 leading to $\mathbf{R}_e(\tilde{A}^1A'')$, the equilibrium geometry of S_1 ketene, and to $\mathbf{R}_{mex}$, the minimum energy point on the S_1-S_0 seam of conical intersection. Following internal conversion onto S_0 near $\mathbf{R}_{mex}$, the barrierless paths leading to $\mathbf{R}_e(\tilde{X}^1A_1)$, the equilibrium geometry of ground-state ketene, were found.

I. Introduction

The photodissociation of ketene

$$H_2CCO(S_0 = X^1A_1) + h\nu \rightarrow H_2CCO(S_1 = {}^1A'') \rightarrow H_2CCO(S_0) \rightarrow H_2CCO(T_1 = {}^3A'') \rightarrow {}^3CH_2 + CO(X^1\Sigma^+) \quad (1)$$

has been the object of considerable experimental interest.[1−3] This interest is due in part to the opportunity to observe a specifically quantum mechanical effect, the stepwise increase in the rate constant with increasing energy, in the unimolecular decomposition of an optically prepared reactant.[1] In an attempt to reproduce the detailed steplike structure observed in the experiments,[1] the microcanonical dissociation rate constant for vibrationally excited ketene on T_1 was determined.[4] These calculations, which utilized a novel method[5] for calculating the cumulative reaction probability, did not prove successful. This has motivated theoretical studies of the factors governing the microcanonical analysis,[6] including the nonadiabatic processes that precede dissociation on T_1.[7]

We will consider the electronic structure aspects of the internal conversion, $S_1 \rightarrow S_0$, focusing on the S_1-S_0 seam of conical intersection, likely the key region for the internal conversion. Knowledge of the energetics and interstate couplings in the vicinity of the seam of conical intersection is essential for a reliable treatment of the internal conversion. The precise determination of these quantities represents the most significant contribution of this work. The $S_1 \rightarrow S_0$ internal conversion has been considered previously.[7] The present investigation extends and complements that study, providing a more precise picture of the nonadiabatic interactions in the vicinity of the seam of conical intersection. These electronic structure data can be used to describe the dynamics of the internal conversion. Previously,[11,12] ab initio electronic structure data concerning conical intersections have been incorporated into the description of nonadiabatic dynamics. The present approach, by exploiting recent methodological and formal advances in the description of conical intersections[8−10] that emphasize information obtained on the seam of conical intersection itself, gains important computational advantages when compared with previous techniques for generating these data. Demonstrating the utility of these generally applicable techniques for describing conical intersections in polyatomic molecules (with more than three atoms) is a second key aspect of this work.

Here the energy minimized projection of the seam of conical intersection is determined in the region of the minimum energy point on the seam. In the vicinity of this portion of the seam, the adiabatic energies, $E_I(\mathbf{R})$, and the derivative coupling, $f_\tau^{IJ}(\mathbf{R}) = \langle \Psi_I(\mathbf{r};\mathbf{R}) | (\partial/\partial\tau) \Psi_J(\mathbf{r};\mathbf{R}) \rangle_{\mathbf{r}}$ where $\Psi_I(\mathbf{r};\mathbf{R})$ is an adiabatic electronic state and τ is an internal coordinate, are determined and an approximate diabatic representation, $\Psi_I^d(\mathbf{r};\mathbf{R})$, which rigorously removes the singularity in the derivative coupling, is developed. The complete elimination of the singularity in the derivative coupling at the conical intersection is essential if the diabatic basis is to be of practical computational value. These computed quantities are compared with the analogous results deduced from the characteristic parameters[8] of a point of conical intersection. The characteristic parameters enable, identification of the two modes that evince the conical nature of the intersection, determination of the energy and singular part of the derivative coupling near the conical intersection, and computation of a transformation to diabatic states that rigorously removes the singularity in the derivative coupling. These calculations are an essential prerequisite to developing coupled potential energy surfaces to describe the internal conversion and represent, to our knowledge, the first time a seam of conical intersection has been described at this level of detail in a molecule of this size.

Section II outlines the electronic structure treatment. Section III presents the results of the calculations, principally the locus of the seam of conical intersection, and the analysis of that seam based on the characteristic parameters. Also presented are the energetics along pathways leading to the seam of conical intersection and the possible outcomes of a conical intersection

* Supported in part by DOE−BES Grant DE-FG02-91ER14189.

10.1021/jp9910136 CCC: $18.00
Published on Web 08/03/1999

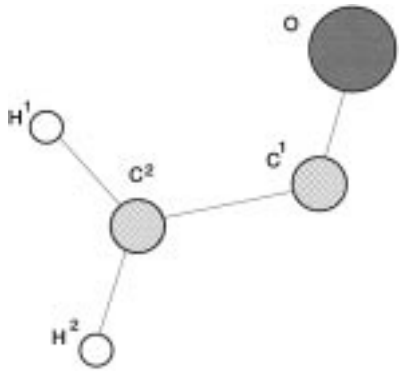

Figure 1. Planar ketene with atomic labeling as in the text.

induced internal conversion. The detailed representation of the seam of conical intersection and the local diabatic basis in terms of the characteristic parameters is presented in the Appendix. Section IV summarizes and discusses directions for future investigations.

II. Theoretical Approach

A. Electronic Structure Treatment. The electronic structure calculations reported in this work were carried out in C_1 symmetry for the $1,2^1$A states. Although important portions of the seam of conical intersection considered here have C_s symmetry (all atoms coplanar, Figure 1), a C_1 symmetry treatment is required to describe the conical nature of the intersection. In this work, C_s symmetry will refer to configurations with all atoms coplanar, although noncoplanar C_s symmetry configurations with two equivalent hydrogens also exist.

Each adiabatic wave function is expanded as $\Psi_I(\mathbf{r};\mathbf{R}) = \sum_{\alpha=1}^{N^{CSF}} c_\alpha^I(\mathbf{R})\psi_\alpha(\mathbf{r};\mathbf{R})$ where the $\mathbf{c}^I(\mathbf{R})$ satisfy $[\boldsymbol{H}(\mathbf{R}) - E_I(\mathbf{R})]\mathbf{c}^I(\mathbf{R}) = \mathbf{0}$ and $\boldsymbol{H}(\mathbf{R})$ is the electronic Hamiltonian matrix in the ψ_α, configuration state function (CSF),[13] basis. The $\Psi_I(\mathbf{r};\mathbf{R})$ were approximated by second-order configuration interaction (SOCI)[13] wave functions—linear combinations of all CSFs arising from zero-, one-, and two-electron excitations from the active orbitals to all the virtual orbitals using the following partitioning of the molecular orbitals, [1a−4a; 8] {5a−12a; 14}, or in C_s symmetry [1a′−4a′; 8] {5a′−10a′, 1a″−2a″ ;14}. Here the square brackets [ ] denote the core orbitals, the 1s orbital of the carbons and of the oxygen and the 2s orbital of oxygen, kept fully occupied in the SOCI expansion; the curly brackets { } denote the active orbitals; and the number of electrons in the corresponding molecular orbital set follows the semicolon. In the ketene region the ground $\tilde{X}^1A_1$ state is dominated by the closed shell configuration {5a′−9a′, 1a″−2a″; 14} and the $\pi \rightarrow \sigma^*$ excitation, 2a″ → 10a′, leads to the $\tilde{A}^1A''$ state.

The molecular orbitals were determined from a complete active space (CAS)[14] state-averaged multiconfigurational self-consistent field (SA-MCSCF)[15] procedure. To facilitate convergence of the SA−MCSCF procedure, the core and active spaces were redefined, for the orbital optimizations only, using C_s symmetry notation, as $[1a'-7a']^{14}$ $\{8a'-10a', 1a''-2a''\}^8$. With an eye toward photochemical processes involving S_2, in the SA-MCSCF procedure three ^{1}A states were averaged with weights 0.51, 0.5, and 0.49. Standard Dunning−Huzinaga double−ζ plus polarization (DZP) basis[16] sets, C[9s5p1d]/(4s2p1d), O[9s5p1d]/(4s2p1d), and H[4s1p]/(2s1p), were used, yielding a SOCI treatment consisting of 666 450 CSFs.

This SOCI expansion excludes the oxygen 2s correlation. As shown below, it is adequate for this treatment, which focuses on the near ketene region, where the effects of the differential oxygen 2s correlation are limited. The sequel to this work will consider S_0 and S_1 over a more extended range of nuclear coordinates. That treatment will include the oxygen 2s correlation and a larger contracted Gaussian basis set.

All points on the 1^1A-2^1A surface of the conical intersection are degenerate to <1 cm^{-1} and were determined at the SOCI level using an analytic gradient driven algorithm,[17] in which some geometrical parameters are constrained and the rest optimized to minimize the energy at the crossing. Unless otherwise noted, energy minimization—which need not preserve C_s symmetry—was achieved through the use of a quasi-second-order procedure described previously.[17,18]

III. Results and Discussion

A. Comparison with Previous Results. The equilibrium geometry of the $\tilde{X}^1A_1$ state, $\mathbf{R}_e(\tilde{X}^1A_1)$, which has C_{2v} symmetry and that of the $\tilde{A}^1A''$ state which has only C_s symmetry, $\mathbf{R}_e(\tilde{A}^1A'')$, are reported, in the first two rows, in Table 1. See also Figure 1. For $\mathbf{R}_e(\tilde{X}^1A_1)$, R_e(C−O) = 1.165(1.160) Å, R_e(C−C) = 1.322(1.312) Å, R_e(C−H) = 1.079(1.076) Å, and $\angle_e$HCH = 121.7°(121.8°), in good accord with very high level ab initio results given parenthetically.[19] For $\mathbf{R}_e(\tilde{A}^1A'')$, R_e(C−O) = 1.194(1.194) Å, R_e(C−C) = 1.440(1.426) Å, and $\angle_e$CCO = 128.8° (130.6°) in good agreement with previous equations of motion coupled with cluster singles and doubles (EOM-CCSD) determination[7] again given parenthetically. Comparing $\mathbf{R}_e(\tilde{X}^1A_1)$ and $\mathbf{R}_e(\tilde{A}^1A'')$ shows that at least ∠CCO and R(C−C) must be considered in any model of the internal conversion. On the other hand, for CO($X^1\Sigma^+$), R_e(C−O) = 1.1283 Å,[20] and for CH_2($^1A'$), R_e(C−H) = 1.08 Å and $\angle_e$HCH = 102.1°,[21] suggesting that at least the C−O and C−H bond distances will not be crucial to the dynamics.

The computed vertical excitation energy of ketene, $E_{2^1A}(\mathbf{R}_e(\tilde{X}^1A_1)) - E_{1^1A}(\mathbf{R}_e(\tilde{X}^1A_1))$, is 4.05 eV, while the adiabatic excitation energy, $E_{2^1A}(\mathbf{R}_e(\tilde{A}^1A'')) - E_{1^1A}(\mathbf{R}_e(\tilde{X}^1A_1))$, is 2.664 eV. These results are in satisfactory accord with the vertical (adiabatic) excitation energy, 3.92(2.73), 3.98(2.81), and 3.56(2.44) eV, obtained at the EOM-CCSD/6-31G(d,p), EOM-CCSD/PVTZ′, and CASPT2[22]/6-31G(d,p), levels respectively. See ref 7 for computational details. The adiabatic excitation energy is also in good accord with the experimental upper bound $T_0(^1A'') < 2.64$ eV.[23] In this work, all energies will be reported relative to $E_{2^1A}(\mathbf{R}_e(\tilde{A}^1A'')) = -152.007\,819\,0$ au. Distances will be expressed in a_0 unless otherwise noted.

$\mathbf{R}_{mex}$, the minimum energy point on the $1^1A - 2^1A$ surface of conical intersection in the near ketene region, is given in Table 1. At $\mathbf{R}_{mex}$, R(C−O) = 1.189(1.215) Å, R(C−C) = 1.538-(1.528) Å, ∠CCO = 116.2° (115.8°), and $E_{1^1A}(\mathbf{R}_{mex}) = E_{2^1A}(\mathbf{R}_{mex}) \equiv E_x(\mathbf{R}_{mex}) = 0.21(0.22)$ eV in good accord with the results of ref 7 given parenthetically.

The above comparisons support the reliability of the present approach. Further comparing $\mathbf{R}_{mex}$, $\mathbf{R}_e(\tilde{A}^1A'')$, and $\mathbf{R}_e(\tilde{X}^1A_1)$ confirms that R(C−C) and ∠CCO must be included in any description of the internal conversion.

We now consider the qualitative or mechanistic description of the internal conversion. In successive subsections, we consider (i) the locus of the seam of conical intersection, (ii) a description of the energetics and interstate couplings in the adiabatic and diabatic bases in the vicinity of the conical intersection seam, (iii) the initial motion on S_1 following (vertical) excitation from S_0 and the accessibility of the seam of conical intersection, and (iv) the motion on S_0 following internal conversion. These data represent an essential first step in constructing a reduced dimensionality model of the internal conversion. We begin by

TABLE 1: Energetics from SOCI Wave Functions

∠CCO	*R*(CO)	*R*(CC)	*R*(C^2H^1)	*R*(CH^2)	∠HCH	∠H^1CC	∠H^1CCO	∠H^2CC	*E*(eV)	*gxh*[c]
					$^1A''$					
180	2.201	2.498	2.040	2.040	121.7	119.4			1.386[a]	
128.8	2.256	2.721	2.041	2.053	120.5	119.4			0[a]	
					1^1A-2^1A					
116.2	2.247	2.906	2.053	2.047	120.1	118.9	0.1	121.0	0.206[b]	0.247(1)
118.7	2.241	2.960	2.054	2.053	126.3	123.7	0.4	123.7	0.294[b]	
119.2	2.241	2.955	2.068	2.052	124.4	109.1	0.8	109.1	0.325[b]	0.256(2)
					1^1A-2^1A *R*(C−C) Constrained					
104.2	2.331	2.35	2.057	2.064	115.6	122.6	27.3	120.1	2.273	0.174
106.0	2.306	2.45	2.057	2.061	116.0	121.2	21.4	119.4	1.533	0.191
108.0	2.289	2.55	2.058	2.058	116.2	120.2	16.7	119.2	0.977	0.204
109.0	2.284	2.60	2.058	2.057	116.4	119.9	14.7	119.4	0.763	0.208(3)
110.0	2.279	2.650	2.058	2.056	116.7	119.7	12.8	119.7	0.581	0.214
111.0	2.272	2.700	2.057	2.055	117.1	119.5	11.0	120.0	0.442	0.227
111.9	2.267	2.75	2.057	2.053	117.6	119.4	8.7	120.7	0.341	0.233
112.0	2.260	2.80	2.056	2.053	118.0	119.5	1.8	122.5	0.274	0.202(4)
116.0	2.240	2.9	2.054	2.047	120.0	118.9	0	121.1	0.206	0.246
120.0	2.225	3.00	2.051	2.043	122.2	118.0	0.2	119.8	0.252	0.283(5)
123.7	2.230	3.1	2.048	2.039	124.6	117.1	0.1	118.3	0.375	0.306
125.3	2.223	3.15	2.046	2.037	126.1	116.3	0	117.6	0.473	0.307
126.5	2.220	3.2	2.045	2.035	127.3	115.7	0	117.0	0.584	0.311
128.3	2.205	3.3	2.042	2.035	129.7	113.5	1.0	116.7	0.835	0.340
129.4	2.193	3.40	2.041	2.032	132.0	113.2	0	114.8	1.104	0.340(6)
129.9	2.189	3.500	2.040	2.031	134.3	112.1	0.1	113.6	1.337	0.354
					1^1A-2^1A ∠CCO Constrained					
97.2	2.340	2.534	2.023	2.026	120.4	123.5	0	116.1	1.672	0.0847
100	2.326	2.574	2.024	2.032	120.7	121.3	0	118.0	1.283	0.0861
102.5	2.313	2.615	2.027	2.036	121.1	119.4	0	119.5	0.971	0.0982
105	2.304	2.664	2.032	2.040	121.5	117.8	0	120.7	0.703	0.118
108	2.291	2.725	2.039	2.043	121.4	116.9	0	121.7	0.445	0.171
110	2.271	2.769	2.044	2.045	121.0	116.9	0	122.1	0.333	0.176
112	2.268	2.814	2.048	2.046	120.7	117.3	0.2	121.9	0.260	0.198
115	2.252	2.880	2.052	2.047	120.4	118.2	0.9	121.4	0.211	0.234
120	2.236	2.973	2.058	2.051	119.0	121.1	2.3	119.2	0.239	0.291
125.2	2.221	3.040	2.065	2.054	116.6	123.5	3.4	115.1	0.355	0.362
135	2.257	3.166	2.079	2.069	109.5	130.7	1.8	106.0	0.833	0.480
142	2.266	3.289	2.094	2.076	105.9	139.3	-6.7	101.4	1.428	0.624

[a] Results at $\mathbf{R}_e(\tilde{X}^1A_1)$ above those at $\mathbf{R}_e(\tilde{A}^1A'')$. [b] $\mathbf{R}_{mex}$ above $\mathbf{R}_{x_{20}}$, $\mathbf{R}_{x_{44}}$, the points on a surface of conical intersection reached using the damped crossing search (see text) from $\mathbf{R}_{p_{20}}$ and $\mathbf{R}_{p_{44}}$, respectively. $\mathbf{R}_{x_{20}}$ above $\mathbf{R}_{x_{44}}$. Number in parentheses at right hand side labels the entry in Table 2. [c] Multiplied by 100.

considering the locus of the seam of conical intersection, in terms of the essential nuclear coordinates *R*(C−C) and ∠CCO.

B. Seam of Conical Intersection. *(i) Symmetry Considerations.* For a general polyatomic molecule, the seam of conical intersection may have dimension $N^{int} - 2$, where $N^{int} = 3N - 6$ and *N* is the number of atoms. Here then the seam may have dimension 7. In the region under consideration, for planar structures, the 1^1A and 2^1A states have $^1A'$ and $^1A''$ symmetry. For these planar structures, there are $N^{int,a'} = 7$($N^{int,a''} = 2$) internal modes of a′ (a″) symmetry so that restricted to the planar structures the intersection seam has dimension $N^{int,a'} - 1 = 6$. These intersections are not conical in C_s symmetry since the $^1A'$ and $^1A''$ states are not coupled by purely a′ modes. These surfaces intersect conically in the full coordinate space. The conical topology exists in a space of dimension 2 consisting, for C_s structures, of one a′ mode and one a″ mode. Finally observe that since for C_s structures the seven internal directions orthogonal to the seam consist of six a′ modes and one a″ mode, the C_s portion of the seam of conical intersection continuously connects with a no-symmetry portion.

ii. Intersecting Seams. Recently, an unexpected locus of points of conical intersection has been found in MH_2[24−26] molecules. For these molecules, the seam of conical intersection consists of two branches, an accidental symmetry-allowed (C_{2v}) branch (e.g., $^{2S+1}A_1 - {}^{2S+1}B_2$) and an accidental same symmetry (C_s) branch (e.g., $1^{2S+1}A' - 2^{2S+1}A'$). These branches in turn intersect at a single point with C_{2v} symmetry.[9] Related confluences have been found in the $2^2E'$ state of Li_3[27] and of Na_3.[28] The seam described below contains both accidental symmetry-allowed and same symmetry portions. Thus, the question naturally arises as to whether the locus reported here represents a single isolated seam or contains portions of two branches that intersect. To distinquish between these alternatives, the magnitude of $\mathbf{t}^{IJ}(\mathbf{R}_x) \equiv \mathbf{g}^{IJ}(\mathbf{R}_x) \times \mathbf{h}^{IJ}(\mathbf{R}_x)$, will be monitored where

$$g_\tau^{IJ}(\mathbf{R}) = (\mathbf{c}^I(\mathbf{R}_x) - \mathbf{c}^J(\mathbf{R}_x))^\dagger \frac{\partial \boldsymbol{H}(\mathbf{R})}{\partial \tau}(\mathbf{c}^I(\mathbf{R}_x) + \mathbf{c}^J(\mathbf{R}_x)) \quad (2a)$$

$$h_\tau^{IJ}(\mathbf{R}) = \mathbf{c}^I(\mathbf{R}_x)^\dagger \frac{\partial \boldsymbol{H}(\mathbf{R})}{\partial \tau}\mathbf{c}^J(\mathbf{R}_x) \quad (2b)$$

$I = 1^1A$ and $J = 2^1A$. $\mathbf{t}^{IJ}(\mathbf{R}_x) = 0$ when $\mathbf{R}_x$ is located at the intersection of two (or more) seams of conical intersection.[29]

iii. Numerical Results. The following analysis considers displacements along *R*(C−C) and ∠CCO from $\mathbf{R}_{mex}$. These displacements preserve C_s symmetry; however, the energy minimization need not. In this region for coplanar geometries, the seam of conical intersection is accidental but symmetry-allowed and either ∠CCO or *R*(C−C) can be used as the seam parameter, β; that is, $\mathbf{R}_x$ becomes $\mathbf{R}_x[\beta]$, with the remaining

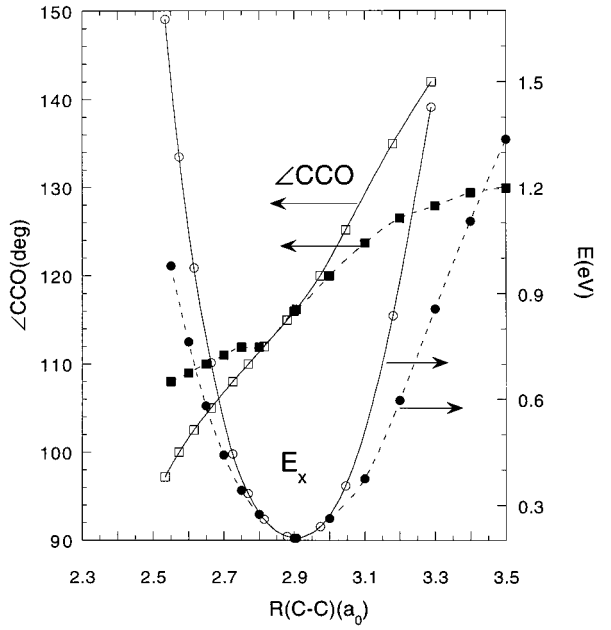

Figure 2. ∠CCO[β] and $E_x(\mathbf{R}_x[\beta])$ plotted vs R(C−C)[β], with β = ∠CCO (solid line, open markers) and with $\beta = R$(C−C) (dashed line, filled markers).

geometrical parameters optimized to minimize $E_x(\mathbf{R}_x[\beta])$. Table 1 and Figure 2 report $\mathbf{R}_x[\beta]$ and $E_x(\mathbf{R}_x[\beta])$. The results are quite illuminating. For 2.8 < R(C−C) < 3.0 and 110° < ∠CCO < 120°, near $\mathbf{R}_{mex,}$ equivalent results are obtained with $\beta = R$(C−C) and β = ∠CCO. [The difference of 0.014(0.013) eV at ∠CCO = 112°(120°) is attributed to convergence issues.] However, significant differences are evident for 2.8 > R(C−C) or R(C−C) > ∼3.2. From Figure 2, it is seen that the optimal solutions for $\beta = R$(C−C) have a much smaller ∠CCO dependence immediately outside this region than those mandated in ∠CCO when ∠CCO is the parameter. Hence, the solutions for R(C−C) > 3.0 and R(C−C) < 2.8 diverge from those with ∠CCO as the parameter. For ∠CCO significantly less than 108°, or 120° < ∠CCO < 130°, the ∠CCO parameterized curve is clearly following a local minimum.

For R(C−C) < 2.8 or ∠CCO > 120°, the molecule is nonplanar. See Table 1. In this regard, note that our results at $\mathbf{R}_x[\beta]$, for $\beta = R$(C−C) = 3.2(3.21), with R(C−O) = 2.220(2.225), ∠CCO = 126.5°(125°), ∠HCC = 115.7°(118°) and $E_x(\mathbf{R}_x[\beta]) - E_x(\mathbf{R}_{mex}) = 0.384(0.370)$ eV are in good accord with those of ref 7 given parenthetically. Agreement deteriorates somewhat for $\beta = R$(C−C) = 2.65(2.65), with R(C−O) = 2.279(2.338), ∠CCO = 110.0°(107°), ∠HCC = 119.7°(119.5°), and $E_x(\mathbf{R}_x[\beta]) - E_x(\mathbf{R}_{mex}) = 0.375(0.41)$ eV. These differences reflect the fact that our result for R(C−C) = 2.65 has no spatial symmetry, a situation apparently not considered in ref 7.

Comparing $\mathbf{R}_{mex}$ and $\mathbf{R}_e(\tilde{A}^1A'')$ with $\mathbf{R}_e(\tilde{X}^1A_1)$, it is seen that leaving the Franck−Condon region on S_1, $\mathbf{R}_e(\tilde{A}^1A'')$ lies "ahead of" $\mathbf{R}_{mex}$. For noncoplanar $\mathbf{R}_x$, one of R(C−C) or ∠CCO is closer to its value at $\mathbf{R}_e(\tilde{X}^1A_1)$, the Franck−Condon region value, than to $\mathbf{R}_e(\tilde{A}^1A'')$. Thus, these noncoplanar $\mathbf{R}_x$ may provide alternative, direct paths to the seam of conical intersection. This point is addressed below.

C. Characterizing the Conical Intersection Region. The propensity for a nonadiabatic transition depends on the energies and nonadiabatic couplings in the vicinity of the conical intersection. As noted in the Introduction, determination of these quantities, to which we now turn, is the key issue in this work. The mathematical basis of this presentation is summarized in the Appendix.

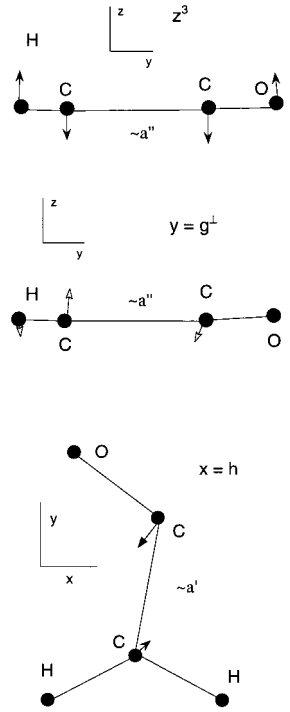

Figure 3. **h**, $\mathbf{g}^{\perp}$, and $\mathbf{z}^3$ for $\mathbf{R}_{x20}$.

The characterization can be provided in either the adiabatic or an approximate diabatic basis. Since the derivative coupling, or its residual in the approximate diabatic basis, is a nine-dimensional vector, tabulation of the electronic structure data can be quite complicated. The fact that the derivative coupling is singular in the adiabatic basis at the conical intersection would appear to be a further complicating factor. The opposite turns out to be the case since the singular part of the derivative coupling is all that is required for all but the most precise treatments. The adiabatic energies and the singular part of the derivative coupling can be described analytically, in terms of a set of characteristic parameters, $\mathbf{g}^{IJ}(\mathbf{R}_x)$, $\mathbf{h}^{IJ}(\mathbf{R}_x)$, and $\mathbf{s}^{IJ}(\mathbf{R}_x) \equiv (\mathbf{g}^I(\mathbf{R}_x) + \mathbf{g}^J(\mathbf{R}_x))/2$ for each conical intersection point, $\mathbf{R}_x$.[8] Here $g^I_\tau(\mathbf{R}_x) = \mathbf{c}^I(\mathbf{R}_x)^\dagger(\partial \boldsymbol{H}(\mathbf{R}_x)/\partial\tau)\mathbf{c}^I(\mathbf{R}_x)$, $\tau = 1 - N^{int}$. The appendix tabulates the characteristic parameters for representative points on the seam.

The above observations concerning the derivative couplings are reflected in the adiabatic-to-diabatic states transformation

$$\begin{pmatrix}\Psi_I^d(\mathbf{r};\mathbf{R})\\ \Psi_J^d(\mathbf{r};\mathbf{R})\end{pmatrix} = \begin{pmatrix}\cos\Phi & -\sin\Phi\\ \sin\Phi & \cos\Phi\end{pmatrix}\begin{pmatrix}\Psi_I(\mathbf{r};\mathbf{R})\\ \Psi_J(\mathbf{r};\mathbf{R})\end{pmatrix} \qquad (3)$$

Near $\mathbf{R}_x$, $\Phi(\mathbf{R})$, determined from either the characteristic parameters or the matrix elements of a component of the electric dipole moment operator, rigorously removes the singularity in the derivative coupling.[30,10]

At each $\mathbf{R}_x$, the vectors $\mathbf{g}^{IJ}$ and $\mathbf{h}^{IJ}$ define the $g-h(\mathbf{R}_x)$ plane. Taking $\mathbf{R}_x$ as the origin, define two Cartesian axes in the $g-h(\mathbf{R}_x)$ plane by $\hat{\mathbf{x}} = \mathbf{h}^{IJ}(\mathbf{R}_x)/||\mathbf{h}^{IJ}(\mathbf{R}_x)||$, $\hat{\mathbf{y}} = \mathbf{g}^{IJ}(\mathbf{R}_x)^{\perp}/||\mathbf{g}^{IJ}(\mathbf{R}_x)^{\perp}||$ where $\mathbf{g}^{IJ}(\mathbf{R}_x)^{\perp} = \mathbf{g}^{IJ}(\mathbf{R}_x) - (\hat{\mathbf{x}}\cdot\mathbf{g}^{IJ}(\mathbf{R}_x))\hat{\mathbf{x}}$, which in turn define polar coordinates (ρ, θ), by $x = \rho\cos\theta$ and $y = \rho\sin\theta$. The importance of the $g-h(\mathbf{R}_x)$ plane is, as noted in the Appendix, that near a conical intersection the derivative coupling with respect θ is the only singular coupling. Thus, it is the preeminent mode for inducing a nonadiabatic transition. The remaining $N^{int} - 1$ directions are largely ignorable, as they are comparatively ineffective in inducing nonadiabatic transitions.

A $g-h$ plane is illustrated in Figure 3, which presents for

the $\mathbf{R}_x$ denoted $\mathbf{R}_{x_{20}}$ in Table 1, the $\hat{\mathbf{x}}$ and $\hat{\mathbf{y}}$ spanning $g-h(\mathbf{R}_{x_{20}})$, and a vector $\mathbf{z}^3$, one of the seven independent vectors perpendicular to $g-h(\mathbf{R}_{x_{20}})$. The significance of $\mathbf{z}^3$ is discussed below. Consistent with the previous discussion, $\mathbf{g}^{IJ}(\mathbf{R}_x)^{\perp}$ has (largely) a″ symmetry and represents a twisting of the C−C moiety out of the molecular plane, while $\mathbf{h}^{IJ}(\mathbf{R}_x)$ preserves C_s symmetry and represents a twisting of the C−C moiety in the molecular plane.

Figure 4 reports the essential aspects of our characterization of the adiabatic and diabatic states and their interconversion focusing on, as typical, $C_\rho(\mathbf{R}_{x_{20}})$ $\rho = 0.05$, the circle in the $g-h(\mathbf{R}_{x_{20}})$ plane with radius 0.05 centered at $\mathbf{R}_{\mathbf{x}_{20}}$. Figure 4a reports the computed, adiabatic energies, E_K, $K = 1^1$A and 2^1A, and singular part of the derivative coupling $(1/\rho)f_\theta$ (the superscripts IJ are suppressed here and below) and compares them with the perturbative results, E_I^{p1} and f_θ^{p1}, requiring only the characteristic parameters,[8] and the higher order estimate f_θ^{p2}. See eqs A1 and A3 in the Appendix. The agreement between E_I and E_1^{p1} and between f_θ and f_θ^{p1} is quite good and improves for f_θ and f_θ^{p2}. However, determination of the higher order estimate f_θ^{p2} requires data in the vicinity of, not just at, the conical intersection.

The data in Figure 4a exhibit C_s symmetry centered around $\theta \sim 67°$. At this coplanar configuration, $\partial/\partial\theta$ has a″ symmetry and f_θ is minimized but not zero. The largest derivative couplings occur for the C_1 structures symmetrically placed around $\theta \sim 67°$. These results are in contradistinction to the frequent assumption that in this region the largest coupling is due to a pure a″ mode.[7] In any case, at least one a″ degree for freedom needs to be incorporated into a realistic description of this process.

Figure 4b reports f_ρ and f_{z^3}, the largest of the f_{z^i}. The key point in Figure 4b is the uniformly small values of these couplings despite the proximity to $\mathbf{R}_x$. In fact, from the ordinate scale, the minimum value of $(1/\rho)f_\theta$ is far larger than any of these couplings. Note that as required by symmetry, $f_\rho(\theta \sim 67°) = 0$. Interestingly, z^3 is largely an a″ mode, serving to confirm/illustrate the preceding symmetry analysis which permitted only one a″ mode to contribute to the singular derivative coupling, despite the fact that the states in question are of ^{1}A′ and ^{1}A″ symmetry at $\mathbf{R}_x$. The good agreement between the f_θ and f_θ^{p1} and small size of the remaining derivative couplings demonstrates that as a practical matter the *derivative couplings need not be computed in the vicinity of a conical intersection point provided the characteristic parameters are known.*

The analysis in the next three figures is central to this work since it considers the diabatic basis determined from the matrix elements molecular property operator.[31] Figure 4c begins the analysis reporting $\mu_{IJ}^x \equiv \langle\Psi_I(\mathbf{r};\mathbf{R})|\hat{\mu}_x(\mathbf{r})\Psi_J(\mathbf{r};\mathbf{R})\rangle_{\mathbf{r}}$, where $\hat{\mu}_x(\mathbf{r})$ is the x component of the electronic part of the dipole moment operator and compares it with the corresponding perturbative result $\mu_{IJ}^{x(p)}$. See eq A9. Also reported in that figure are $\Phi^{(p1)}$ and $\Phi^{\mu x}$, the Φ determined from the characteristic parameters using eq A6 and from μ_{IJ}^x using eq A8, respectively. Since

$$f_\theta^{(p)} \equiv \frac{\partial}{\partial\theta}\Phi^{(p)} \xrightarrow[\rho\to 0]{} f_\theta$$

the agreement between $\Phi^{(p)}$ and $\Phi^{\mu x}$ (see also Figure 4e below) illustrates the formal result that the transformation to diabatic states generated by $\Phi^{\mu x}$ removes the singular part of the derivative coupling,[32,10]

$$\frac{\partial}{\partial\theta}\Phi^{\mu^x} \xrightarrow[\rho\to 0]{} f_\theta$$

Because of the ease with which $\Phi^{\mu x}$ is determined away from a conical intersection, it is a popular means of obtaining diabatic states. The general result

$$\frac{\partial}{\partial\theta}\Phi^{\mu^x} \xrightarrow[\rho\to 0]{} f_\theta$$

which differs somewhat from previous assertions,[33] is therefore quite important since it guarantees the desired behavior of $\Phi^{\mu x}$ at the conical intersection.

Parts d and e of Figure 4 continue the analysis of the diabatic basis determined by $\Phi^{\mu x}$. Figure 4d considers the energy and dipole moment in the diabatic basis, reporting $H_{IJ}^d(\mathbf{R}) \equiv \langle\Psi_I^d(\mathbf{r};\mathbf{R})|H(\mathbf{r};\mathbf{R})\Psi_J^d(\mathbf{r};\mathbf{R})\rangle_{\mathbf{r}}$ and $\mu_{IJ}^{xd} \equiv \langle\Psi_I^d(\mathbf{r};\mathbf{R})|\hat{\mu}_x(\mathbf{r})\Psi_J^d(\mathbf{r};\mathbf{R})\rangle_{\mathbf{r}}$. Note that while μ_{IJ}^{xd} is approximately constant, $H_{IJ}^d(\mathbf{R})$ exhibit a $\cos(\theta + \sigma_{IJ})$ dependence. Further insight into these results is obtained from Figure 4e, which reports $E_I(\mathbf{R})$, f_θ, $f_\theta^{(p1)}$, and $H_{IJ}^d(\mathbf{R})$. Note the good agreement between f_θ and $f_\theta^{(p1)}$ despite the large grid size, 30°. Note too that $E_I(\mathbf{R})$ and $H_{11}^d(\mathbf{R})$ agree except where f_θ is large, that is, for $\theta \sim -22°$ and 157°. In those regions, the roles of $H_{11}^d(\mathbf{R})$ and $H_{22}^d(\mathbf{R})$ switch, owing to the avoided intersection of the adiabatic curves. Parts d and e of Figure 4 illustrate the formal result (see Appendix) that, as for the derivative couplings, *the adiabatic-to-diabatic states transformation and the associated energetics in the vicinity of the conical intersection are obtained using only the characteristic parameters and the matrix elements of a property operator at the conical intersection.*

Finally note from Table 1 that although $|\mathbf{t}^{IJ}(\mathbf{R}_x[\angle\text{CCO}])|$ decreases with decreasing ∠CCO, no intersecting seams, at reasonable energies, are indicated.

D. Motion on the 2^1A′ Potential Energy Surface. Following the initial excitation, $S_0 \rightarrow S_1$, the system evolves on the 2^1A potential energy surface until it makes the nonadiabatic transition onto the 1^1A potential energy surface. While both $E_{2^1\text{A}}(\mathbf{R}_{\text{mex}})$ and $E_{2^1\text{A}}(\mathbf{R}_e(\tilde{\text{A}}^1\text{A}''))$ are exoergic relative to the initial excitation, the barrier(s) on the 2^1A potential energy surface may make one or both of these regions inaccessible. To address this point, the following series of calculations, which is also useful in determining the geometric parameters essential for the description of this process, was performed. Starting at $\sim\mathbf{R}_e(\tilde{\text{X}}^1\text{A}_1)$, a gradient directed path, $\mathbf{R}_{p_i}$—the path obtained by following the (scaled) energy gradient $\mathbf{g}^I$—was followed on the 2^1A potential energy surface. See parts a and b of Figure 5. The oscillations in, for example, $R(\text{C}^2-\text{H})$ are the result of the scaling of the gradient and do not, in this work, affect the conclusions. From selected points on the path, $\mathbf{R}_{p_i}$, $i = 20$ and 44, a search was performed for a point on the $1^1\text{A}-2^1\text{A}$ seam of conical intersection, $\mathbf{R}_{x_i}$, with the energy minimization implicit in the algorithm[18] heavily damped. The goal of this procedure is to locate a "nearby" point of conical intersection without having to map large portions of the intersection seam. The $\mathbf{R}_{x_i}$, $i = 20$ and 44, obtained in this manner are reported in Table 1. Linear synchronous transit paths between $\mathbf{R}_{p_i}$ and $\mathbf{R}_{x_j}$ were computed. A second gradient-directed path chosen to initially sample noncoplanar structures was determined. See parts c and d of Figure 5. Finally note that the "location" of the "vertical" excitation onto S_1 may depend on the photon energy so that this analysis is no substitute for a careful treatment of the nuclear dynamics.

From parts a and b of Figure 5 and Table 1, its seen that the gradient directed path on S_1 starting from $\mathbf{R}_e(\tilde{\text{X}}^1\text{A}_1)$ leads to $\mathbf{R}_e(\tilde{\text{A}}^1\text{A}'')$, rather than to the seam of conical intersection. This result is rationalized by noting that $\mathbf{R}_{x_{20}}$ and $\mathbf{R}_{x_{44}}$ are quite similar and differ little from $\mathbf{R}_{\text{mex}}$. For these $\mathbf{R}_{x_i}$, $R(\text{C}-\text{C})$ is $\sim 0.2a_0$

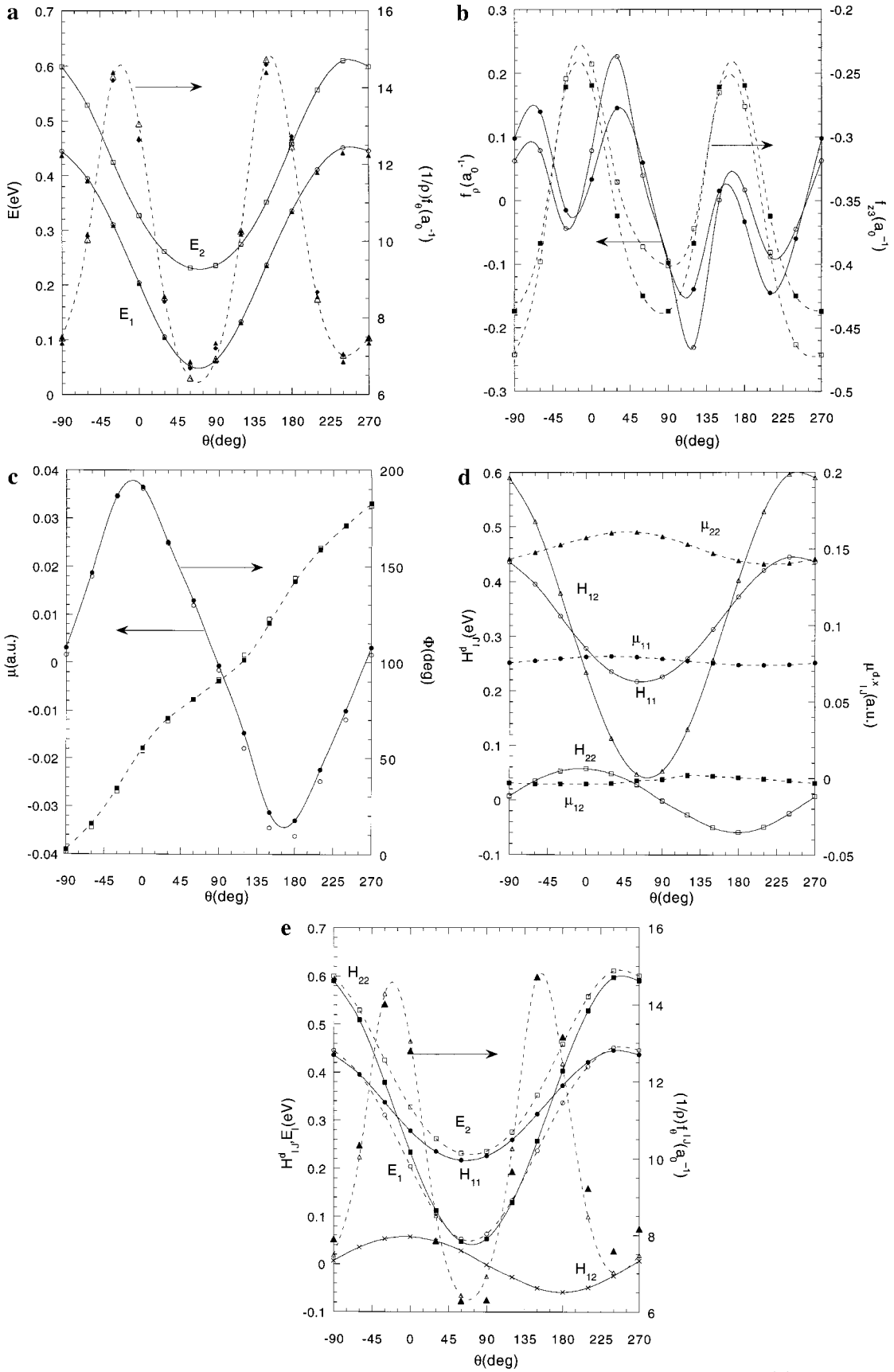

Figure 4. For $\mathbf{R}_{x_{20}}$, $\rho = 0.1$ (a) $E_1{}^1\mathrm{A}$ (open circles), $E_2{}^1\mathrm{A}$ (open squares), $(1/\rho)f_\theta$ (open triangles), compared with $E1_1^{(p1)}\mathrm{A}$ (filled circles), $(1/\rho)f_\theta^{p1}$ (filled triangles), $(1/\rho)f_\theta^{p2}$ (filled diamonds); (b) f_ρ (open circles, solid line) and f_{z^3} (open squares, dashed line) compared with the results of a perturbative fit (filled markers); (c) μ_{IJ}^x (filled circles) and $\Phi^{\mu x}$ (filled squares), compared with the analogous results based on the perturbation theory using the characteristic parameters, $\mu_{IJ}^{x(p)}$ and $\Phi^{\mu x(p)}$ (open markers); (d) H_{IJ}^d, $IJ = 11$ (open circles), 22 (open triangles), 12 (open squares); and $\mu_{IJ}^{x^d}$, $IJ = 11$ (filled circles), 22 (filled triangles), 12 (filled squares); (e) $E_1{}^1\mathrm{A}$ (open circles), $E_2{}^1\mathrm{A}$ (open squares), f_θ (open triangles), f_θ^{p1} (filled triangles), H_{IJ}^d, $IJ = 11$ (filled circles), 22 (filled squares), 12 (×).

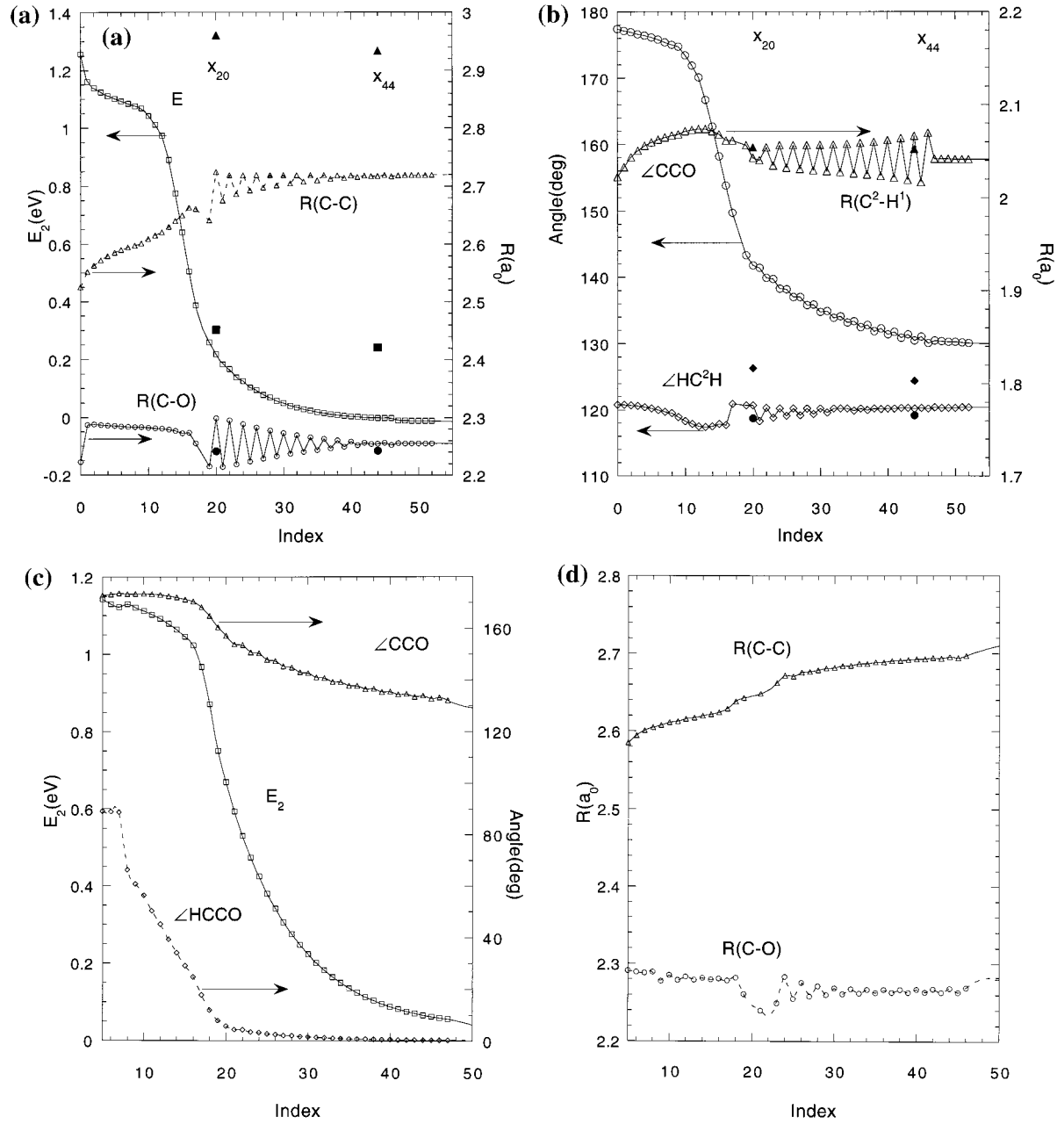

Figure 5. Gradient-directed path on the 2^1A potential energy surface from $\mathbf{R}_e(\tilde{X}^1A_1)$ to $\mathbf{R}_e(\tilde{A}^1A'')$. Shown in (a) are E_{21A} (open squares), R(C−C) (open triangles), and R(C−O) (open circles) and in (b) are $R(C^2-H^1)$ (open triangle), $\angle C^2C^1O$ (open circle), and $\angle HC^2H$ (open diamond). For x_{20} and x_{44} on the seam of conical intersection, the values of E_{2^1A} (filled squares), R(C−C) (filled triangles), R(C−O) (filled circle), $R(C^2-H^1)$ (filled triangle), ∠CCO (filled circle), and $\angle HC^2H$ (filled diamond). For the noncoplanar path shown are in (c) E_{2^1A} (open squares), $\angle C^2C^1O$ (open triangles), and $\angle H^1C^2C^1O$ (open diamonds) and in (d) R(C−C) (open triangles) and R(C−O) (open circles).

greater and ∠CCO is ∼10° smaller than for $\mathbf{R}_e(\tilde{A}^1A')$ so that $\mathbf{R}_e(\tilde{A}^1A')$ lies "ahead of" $\mathbf{R}_{x_i}$ on the gradient-directed path. However, motion in directions perpendicular to this path may access the conical intersection seam prior to reaching $\mathbf{R}_e(\tilde{A}^1A')$. In this regard, Figure 6 considers linear synchronous transit paths, constructed in Cartesian coordinates, plotted as a function of ∠CCO, from $\mathbf{R}_{p_{20}}$ and $\mathbf{R}_{p_\infty} = \mathbf{R}_e(\tilde{A}^1A'')$ respectively to $\mathbf{R}_{x_{20}}$. These results establish the existence of a barrierless path, from p_{20} or p_∞, to x_{20}.

From parts c and d Figure, it is seen that the non-coplanar gradient directed path, which was effectively started with a dihedral $\angle H^1CCO$ of ∼67°, also leads to $\mathbf{R}_e(\tilde{A}^1A'')$. This result can be attributed to the affinity of the 2^1A potential energy surface for coplanarity evidenced in Figure 5c.

Figures 5a−5d confirm the importance of R(C−C) and ∠CCO for nuclear motion S_1. While the paths on S_1 leading from the Franck−Condon region, ∼ $\mathbf{R}_e(\tilde{X}^1A_1)$ to $\mathbf{R}_e(\tilde{A}^1A'')$ are quite reasonable, alternative results were possible. In an analogous treatment of the first excited state of NH_2OH the gradient directed path lead directly to the seam of conical intersection.[34]

E. Motion on the 1^1A potential energy surface following internal conversion. On the upper surface, the conical intersection acts as a funnel, drawing the molecule toward its vertex. However, on the lower surface, it has the opposite effect, directing the molecule to potentially distinct regions of coordinate space. This point is addressed in Figure 7 and Figure 8. Figure 7 illustrates the energetics and $(1/\rho)f_\theta$ and $(1/\rho)f_\theta^{(p1)}$ on $C_\rho(\mathbf{R}_{x_{20}})$ for $\rho = 0.25$. Note that here the agreement between $(1/\rho)f_\theta$ and $(1/\rho)f_\theta^{(p1)}$ is less satisfactory than in Figure 4a, as expected owing to the larger radius. From this circle, three

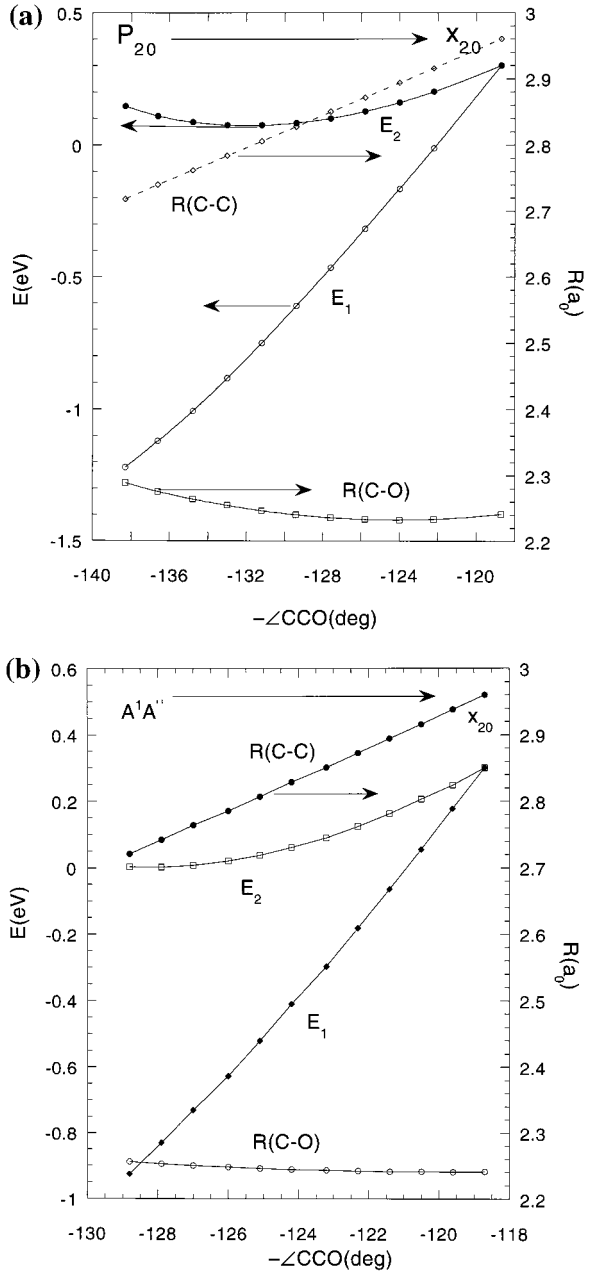

Figure 6. Linear synchronous transit paths to $\mathbf{R}_{x_{20}}$ from (a) $\mathbf{R}_{p_{20}}$ and (b) $\mathbf{R}_e(\tilde{A}^1A'')$. Direction of motion indicated by arrow at the top of each figure.

distinct points were chosen as the origin of gradient directed paths, q_1 which corresponds to a maximum in the derivative coupling and is as discussed earlier a no-symmetry nuclear configuration, and q_2 and q_3 which correspond to high- and low-energy points. While no substitute for a careful dynamical treatment, this analysis serves to identify potentially important aspects of the local topology of the lower potential energy surface.

From Figure 8, it is seen that from points q_1–q_3 the system evolves on S_0 to the region of $\mathbf{R}_e(\tilde{X}^1A_1)$. As previously, the oscillations observed in the bond distances do not affect these conclusions.

F. Mechanistic Implications. The preceding analysis suggests two possible mechanisms for the internal conversion. In the first case, motion perpendicular to the gradient directed path transports the system to the region of the conical intersection at which point internal conversion occurs. Alternatively, the system evolves on S_1 to $\mathbf{R}_e(\tilde{A}^1A'')$, forming an intermediate complex which then ultimately internally converts via the seam of conical intersection. Three coordinates are essential to describe the internal conversion R(C−C), ∠CCO, and an a″ mode like $\mathbf{z}^3$ at $\mathbf{R}_{x_{20}}$.

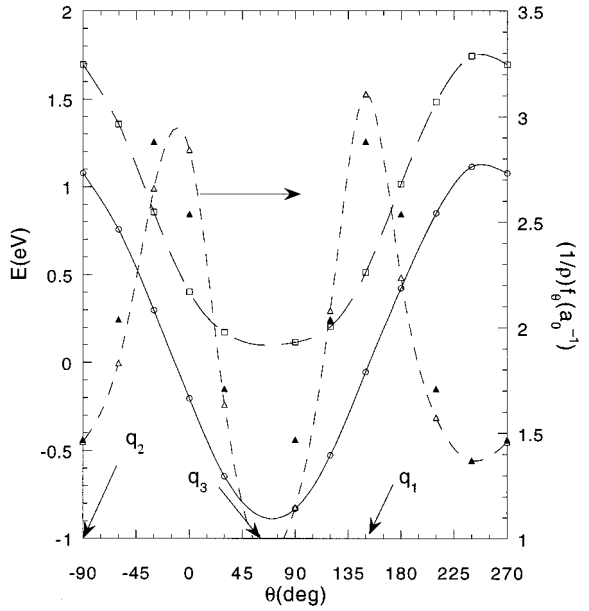

Figure 7. For $C_{0.25}(\mathbf{R}_{x_{20}})$, $E_1{}^1A$ (open circles), $E_2{}^1A$ (open squares), $(1/\rho)f_\theta$ (open triangles), $(1/\rho)f_\theta^{p1}$, (filled triangles). Also indicated are $q_1{}^\theta = 150°$, $q_2{}^\theta = -90°$, and $q_3{}^\theta = 60°$.

Following internal conversion onto S_0, the situation may resemble that found in the standard intermediate complex model.[35,36] The ground state minimum of ketene permits the molecule to repeatedly encounter the S_0-T_1 surface of intersection,[7] leading to dissociation to $^3CH_2 + {}^1CO$.

To determine how the excited wave packet flux is partitioned among these possibilities, a full treatment of the dyamics is required.

IV. Summary and Conclusions

The mechanism of $S_1(^1A'') \rightarrow S_0(^1A')$ internal conversion in ketene, facilitated by the 1^1A-2^1A seam of conical intersection, was considered. Exploiting recent formal and computational advances in the characterization of conical intersections, this work presents a detailed but compact representation of this seam of conical intersection. This analysis provides the basis for the determination of a coupled diabatic states representation of the portions of the 1^1A and 2^1A states relevant to the intersystem crossing, a work currently in progress, or it can be used to refine other representations to these potential energy surfaces.

Energy-minimized projections of the seam of conical intersection with either R(C−C) or ∠CCO held constant were determined. For $R(C-C) \geq 2.8a_0$,which includes $\mathbf{R}_{mex}$ the minimum energy point on the S_1-S_0 seam of conical intersection, the energy-minimized seam has C_s symmetry with all atoms coplanar. However, for $R(C-C) < 2.80$, deviations from coplanarity exist.

It is the immediate vicinity of the conical intersection seam, the key region for inducing a nonadiabatic transition, that is the focus of this work. A compact representation of the energies and the largest part of the derivative couplings is efficiently determined from the characteristic parameters. In particular, by using the characteristic parameters, one can identify the two modes, one a″ and one a′ mode when the molecule has C_s

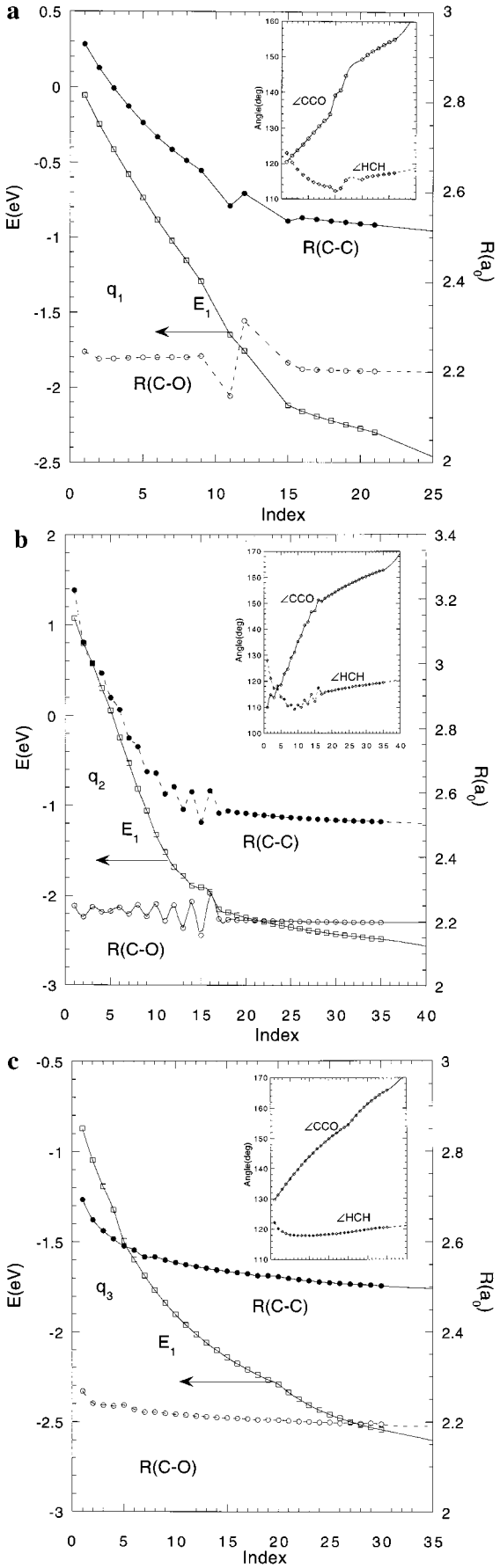

Figure 8. Gradient directed paths from (a) q_1, (b) q_2, and (c) q_3 on the 1^1A potential energy surface, leading to $\mathbf{R}_e(\tilde{X}^1A')$. Shown are E_{1^1A}, (open squares), R(C−C) (open triangles), and R(C−O) (open circles), and in inset are ∠CCO (open circle) and ∠HCH)open diamond).

symmetry, that yield the singular part of the derivative couplings; determine the local energetics; and obtain a transformation to diabatic states that rigorously removes the singularity in the derivative coupling. In the past, the vibronic structure of moderate sized molecules including furan, pyrrole, thiopene,[12] and pyrazine[11] has been treated with the effects of conical intersections described using ab initio electronic structure data. While a description of these complicated vibronic processes was highly successful, the electronic structure treatments required calculation of the wave functions at many points in the immediate vicinity of the conical intersection. The techniques employed in this work, which require information only at the conical intersection, provide significantly enhanced capabilites to incorporate reliable ab initiio data into such treatments[37] of vibronic effects in molecules.

The existence of barriers separating key regions of nuclear coordinate space is a matter of considerable importance. A qualitative representation of the potential energy surface topology for S_0 and S_1, in regions relevant to the internal conversion, was obtained by following gradient directed paths, that is, paths generated by following the (scaled) energy gradient in a stepwise manner. Using this procedure, barrierless paths were identified on S_1 from the Franck−Condon region of the $S_0 \rightarrow S_1$ excitation, leading to $\mathbf{R}_e(\tilde{A}^1A'')$ and $\mathbf{R}_{mex}$. These results demonstrate that the seam of conical intersection is accessible following excitation from S_0. Following internal conversion onto S_0 near $\mathbf{R}_{mex}$, the gradient directed paths lead to $\mathbf{R}_e(\tilde{X}^1A_1)$.

Related questions arise in the photodissociation of isovalent HNCO,

$$\mathrm{HNCO}(S_0 = X^1A') + h\nu \rightarrow \mathrm{HNCO}(S_1 = {}^1A'') \rightarrow \mathrm{HNCO}(S_0) \rightarrow \mathrm{H} + \mathrm{NCO}(X^2\Pi) \quad (4a)$$

$$\mathrm{HNCO}(S_0 = X^1A') + h\nu \rightarrow \mathrm{HNCO}(S_1 = {}^1A'') \rightarrow \mathrm{HNCO}(T_1 = {}^3A'') \rightarrow \mathrm{HN}(X^3\Sigma^-) + \mathrm{CO}(X^1\Sigma^+) \quad (4b)$$

which also has been the object of both theoretical and experimental investigations.[38,39] In future work, a similar analyisis of the internal conversion will be performed for this system.

Appendix

The energies and derivative couplings near $\mathbf{R}_x$, a point of conical intersection of states I and J, can be concisely expressed in terms of the characteristic parameters[8] $\mathbf{g}^{IJ}(\mathbf{R}_x)$, $\mathbf{h}^{IJ}(\mathbf{R}_x)$, and $\mathbf{s}^{IJ}(\mathbf{R}_x) \equiv (\mathbf{g}^J(\mathbf{R}_x) + \mathbf{g}^I(\mathbf{R}_x))/2$ (see eq 2 in the text). Near $\mathbf{R}_x$, it is convenient to use the generalized cylindrical polar coordinates ρ, θ, and z^i with ρ and θ defined in section IIIB and the unit vectors $\hat{\mathbf{z}}^i$ spanning the space of dimension $3N - 8$ orthogonal to the $g-h(\mathbf{R}_x)$ plane. In this work, the $\hat{\mathbf{z}}^i$ are defined in terms of an atom centered cartesian coordinate basis.

i. Energies. In this coordinate system, through first order displacements ($\delta\mathbf{R}$) from $\mathbf{R}_x$

$$E_\pm(\mathbf{R}) \approx E_\pm^{(p1)} \equiv E_I(\mathbf{R}_x) + \mathbf{s}^{IJ}(\mathbf{R}_x)^\dagger \cdot \delta\mathbf{R} \pm \rho q(\theta) \quad (A1)$$

where − corresponds to I, + corresponds to J,

$$q(\theta)^2 = h_x^2 \cos^2\theta + (g_x \cos\theta + g_y \sin\theta)^2 \equiv h^2 \cos^2\theta + g^2 \sin^2(\theta + \beta) \quad (A2a)$$

$$\cos\lambda(\theta) = [h/q(\theta)] \cos\theta \qquad \sin\lambda(\theta) = [g/q(\theta)] \sin(\theta + \beta) \quad (A2b)$$

TABLE 2: Characteristic Parameters for Points on the Seam of Conical Intersection

R			h			2g			s		
x	*y*	*z*	*x*	*y*	*z*	*x*	*y*	*z*	*x*	*y*	*z*
					(1) (116.2, 2.90557)[a]						
0.5219	2.1853	0.0087	−0.0004	0.0001	0.0096	−0.0360	0.0062	−0.0004	−0.0378	0.0065	0.0001
−2.8335	−0.6450	−0.0022	−0.0006	0.0002	0.0287	−0.0524	0.0212	−0.0015	−0.0553	0.0225	0.0000
0.0000	0.0000	0.0000	0.0012	−0.0002	−0.0195	0.1040	−0.0231	0.0008	0.1096	−0.0242	−0.0002
−4.2020	0.8857	0.0014	−0.0001	0.0000	−0.0147	−0.0102	−0.0027	0.0008	−0.0107	−0.0029	0.0000
−3.4698	−2.5911	−0.0001	−0.0001	0.0000	−0.0041	−0.0054	−0.0017	0.0003	−0.0057	−0.0018	0.0001
					$\mu_{11} = -1.056\ 15, \mu_{12} = 0.024\ 00, \mu_{22} = -0.074\ 61$						
					(2) (119.2, 2.9549)						
−1.7501	1.3952	0.0942	0.0026	0.0036	0.0102	0.0198	0.0254	−0.0056	−0.0194	−0.0269	0.0014
−0.4699	−2.9236	−0.0249	0.0055	0.0044	0.0294	0.0409	0.0379	−0.0118	−0.0599	−0.0566	0.0001
0.0000	0.0000	0.0000	−0.0076	−0.0095	−0.0210	−0.0581	−0.0808	0.0109	0.0730	0.0912	−0.0023
1.3525	−3.8703	0.0052	−0.0002	0.0004	−0.0030	−0.0014	0.0056	0.0001	0.0104	0.0088	0.0011
−2.3059	−3.8710	0.0144	−0.0003	0.0012	−0.0155	−0.0011	0.0118	0.0063	−0.0041	−.0166	−0.0003
					$\mu_{11} = 0.123\ 00, \mu_{12} = -0.001\ 64, \mu_{22} = 0.047\ 09$						
					(3) (109.0, 2.60)						
0.1835	2.2149	0.8258	0.0083	−0.0020	−0.0092	−0.0538	−0.0129	−0.0135	−0.0672	−0.0083	0.0050
−2.5024	−0.5661	−0.1212	0.0183	−0.0044	−0.0069	−0.0404	0.0301	−0.0331	0.0463	0.0643	0.0023
0.0000	0.0000	0.3000	−0.0306	0.0050	0.0115	0.0988	−0.0240	0.0223	0.0331	−0.0599	−0.0215
−3.8643	0.9513	−0.4026	0.0019	0.0019	0.0080	−0.0053	0.0044	0.0140	−0.0088	0.0005	−0.0022
−3.2564	−2.3600	0.5451	0.0021	−0.0005	−0.0034	0.0007	0.0025	0.0102	−0.0034	0.0035	0.0165
					$\mu_{11} = -0.710\ 93, \mu_{12} = -0.421\ 74, \mu_{22} = -0.421\ 41$						
					(4) (112.0, 2.80)						
0.3716	2.2292	0.3166	0.0028	0.0006	0.0070	−0.0343	0.0039	−0.0010	−0.0485	0.0051	−0.0036
−2.7193	−0.6056	0.0193	0.0006	−0.0008	0.0257	−0.0515	0.0190	−0.0016	−0.0314	0.0356	−0.0054
0.0000	0.0000	0.3000	−0.0056	0.0012	−0.0158	0.0988	−0.0199	0.0062	0.0982	−0.0369	0.0092
−4.0797	0.9222	−0.1907	0.0017	−0.0007	−0.0122	−0.0077	−0.0012	−0.0035	−0.0110	−0.0016	−0.0013
−3.4357	−2.5280	0.0992	0.0005	−0.0002	−0.0047	−0.0052	−0.0017	−0.0001	−0.0073	−0.0022	0.0011
					$\mu_{11} = -1.037\ 98, \mu_{12} = -0.020\ 28, \mu_{22} = -0.106\ 59$						
					(5) (120.0,3.00)						
0.6451	2.1297	−0.0219	0.0055	−0.0018	0.0112	−0.0349	0.0096	0.0080	−0.0285	0.0090	0.0017
−2.9204	−0.6839	−0.0423	0.0079	−0.0043	0.0296	−0.0487	0.0215	0.0185	−0.0728	0.0107	0.0025
0.0000	0.0000	−0.1000	−0.0152	0.0047	−0.0213	0.1017	−0.0260	−0.0166	0.1158	−0.0151	−0.0047
−4.2673	0.8590	0.0606	0.0011	0.0011	−0.0158	−0.0121	−0.0035	−0.0084	−0.0096	−0.0031	0.0001
−3.5058	−2.6408	−0.0759	0.0006	0.0003	−0.0037	−0.0059	−0.0016	−0.0016	−0.0048	−0.0014	0.0004
					$\mu_{11} = -1.050\ 62, \mu_{12} = -0.120\ 90, \mu_{22} = -0.067\ 52$						
					(6) (129.4,3.40)						
0.9419	1.9807	−0.0555	−0.0044	0.0172	0.0134	−0.0141	0.0508	−0.0156	−0.0029	0.0115	0.0005
−3.2984	−0.8219	−0.0287	0.0004	0.0100	0.0306	−0.0028	0.0331	−0.0414	−0.0875	−0.0145	0.0021
0.0000	0.0000	−0.1000	0.0142	−0.0246	−0.0240	0.0430	−0.0733	0.0280	0.0966	0.0049	−0.0028
−4.5299	0.8030	0.0702	−0.0069	−0.0021	−0.0157	−0.0175	−0.0086	0.0226	−0.0041	−0.0016	0.0001
−3.6814	−2.8165	−0.0932	−0.0033	−0.0005	−0.0043	−0.0087	−0.0020	0.0064	−0.0021	−0.0003	0.0001
					$\mu_{11} = -0.743\ 545\ 28, \mu_{12} = 0.278\ 137\ 19, \mu_{22} = 0.03929390$						

[a] (∠CCO, *R*(C−C)).

$l_w = \mathbf{l}^{IJ}(\mathbf{R}_x)\cdot\hat{\mathbf{w}}$ for $w = x, y, z$ and $\mathbf{l}^{IJ} = \mathbf{g}^{IJ}$, $\mathbf{h}^{IJ}$, $\mathbf{s}^{IJ}$. From eqs A1 and A2, we have the important result that the $g-h(\mathbf{R}_x)$ plane contains all the linear part of the energy difference, $E_+(\mathbf{R}) - E_-(\mathbf{R})$.

ii. Derivative Couplings and Diabatic States. Near $\mathbf{R}_x$, the leading terms in a perturbative expansion of $\mathbf{f}^{JI}(\mathbf{R})$ are[40,8]

$$f_\theta^{JI}(\mathbf{R}) \cong \left[1/2\,\frac{\mathrm{d}}{\mathrm{d}\theta}\lambda(\theta)\right] + \left[\frac{\rho}{2}\frac{\mathrm{d}}{\mathrm{d}\theta}\left(\frac{m_\rho(\theta)}{q(\theta)}\right) + \sum_i \frac{z^i}{2}\frac{d}{d\theta}\left(\frac{m_{z^i}(\theta)}{q\theta}\right)\right] \equiv f_\theta^{(\mathrm{p1}),JI}(\mathbf{R}) + f_\theta^{(\mathrm{p2}),JI}(\mathbf{R}) \equiv f_\theta^{(\mathrm{p}),JI}(\mathbf{R}) \tag{A3a}$$

$$f_\rho^{JI}(\mathbf{R}) \cong m_\rho(\theta)/(2q(\theta)) \equiv f_\rho^{(\mathrm{p}),JI}(\mathbf{R}) \tag{A3b}$$

$$f_{z^i}^{JI}(\mathbf{R}) \cong m_{z^i}(\theta)/(2q(\theta)) \equiv f_{z^i}^{(\mathrm{p}),JI}(\mathbf{R}) \tag{A3c}$$

where

$$\frac{\mathrm{d}\lambda}{\mathrm{d}\theta} = \frac{gh\,\sin(\beta + \pi/2)}{q^2(\theta)} \tag{A4}$$

$$m_w(\theta) = \sum_{i=1}^{K_w}[a_i^w p_i^{aw}(\theta) + b_i^w p_i^{bw}(\theta)] = q(\theta) f_w^{JI} \qquad w = z \text{ or } \rho \tag{A5a}$$

$K_z = 2$, $K_\rho = 3$,

$$p_n^{aw} = \cos^l\theta\,\sin^k\theta\,\sin\lambda(\theta) \qquad p_n^{bw} = \cos^l\theta\,\sin^k\theta\,\cos\lambda(\theta) \tag{A5b}$$

and $(w,n,l,k) = (z,1,1,0)$ and $(z,2,0,1)$ and $(\rho, 1,2,0)$, $(\rho, 2,0,2)$, and $(\rho, 3,1,1)$.

At $\mathbf{R}_x$, only $(1/\rho)f_\theta^{IJ}$ is singular so that the singular part of the derivative coupling can be treated analytically. Equations A3 and A5 enable compact expressions for the nonsingular components of the derivative coupling at $\mathbf{R}_x$ to be obtained by fitting f_w^{IJ} along a small loop surrounding that point.[41]

Near $\mathbf{R}_x$, the transformation angle (Φ) to a diabatic basis (eq 3 in text) is approximated by $\Phi^{(\mathrm{p})}(\mathbf{R})$ with

$$-\Phi^{(p)}(\mathbf{R}) = \lambda(\theta)/2 + [\rho m_\rho(\theta)/(2q(\theta)) + \sum_i z^i m_{z^i}(\theta)/q(\theta)] \equiv -\Phi^{(p1)}(\mathbf{R}) - [\Phi^{(p2)}(\mathbf{R})] \quad \text{(A6)}$$

The derivative coupling in the diabatic basis

$$f_\tau^{d,IJ} = f_\tau^{IJ} - \frac{\partial \Phi^{(p)}}{\partial \tau} \equiv f_\tau^{IJ} - f_\tau^{(p),IJ} \quad \text{(A7)}$$

is negligible near the conical intersection.[41]

iii. Diabatic States and Molecular Properties. Since only the $g-h$ plane, rather than the individual $\mathbf{g}^{IJ}$ and $\mathbf{h}^{IJ}$, is uniquely defined,[29] the angle Φ is arbitrary up to a constant offset. This complicates the synchronization of the Φ at different $\mathbf{R}_x$. This problem can be avoided using a transformation to diabatic states that is uniquely defined and is equally effective in removing the singular part of the derivative coupling at $\mathbf{R}_x$. This is generated by $\Phi = \Phi^A$ (ref 32) where

$$\tan 2\Phi^A(\mathbf{R}) = \frac{A_{ij}(\mathbf{R})}{\Delta A_{IJ}(\mathbf{R})} \quad \text{(A8)}$$

with $A_{IJ}(\mathbf{R}) = \langle \Psi_I(\mathbf{r};\mathbf{R})|A(\mathbf{r})\Psi_J(\mathbf{r};\mathbf{R})\rangle_\mathbf{r}$ and $\Delta A_{IJ}(\mathbf{R}) \equiv (A_{II}(\mathbf{R}) - A_{JJ}(\mathbf{R}))/2$. Here $A(\mathbf{r})$ is any Hermitian operator for which $\Delta A_{IJ}(\mathbf{R})$ and $A_{IJ}(\mathbf{R})$ do not simultaneously vanish at $\mathbf{R}_x$.[32]

Near $\mathbf{R}_x$, explicit computation of $\mathbf{A}(\mathbf{R})$ and, hence, of the wave functions, can be avoided since $\mathbf{A}(\mathbf{R})$ is well approximated by[32]

$$\mathbf{A}^{(p)}(\theta) = (A_{II} + A_{JJ})/2\mathbf{I} + \boldsymbol{\sigma}_x(\Delta A_{IJ} \sin\lambda + A_{IJ}\cos\lambda) + \boldsymbol{\sigma}_z(\Delta A_{IJ}\cos\lambda - A_{IJ}\sin\lambda) \quad \text{(A9)}$$

where $\boldsymbol{\sigma}$ are the Pauli matrices. The Φ obtained from $\mathbf{A}^{(p)}$ is denoted $\Phi^{A,(p)}$.

Thus, knowledge of the characteristic parameters and the relevant operator matrix elements at the conical intersection is sufficient to determine the energies, the largest part of the derivative coupling and the diabatic states near the conical intersection. Table 2 reports the characteristic parameters and matrix elements of $\mu_x(\mathbf{r})$ for selected $\mathbf{R}_x$ in Table 1.

References and Notes

(1) Kim, S. K.; Lovejoy, E. R.; Moore, C. B. *Science* **1992**, *256*, 1541.
(2) Kim, S. K.; Lovejoy, E. R.; Moore, C. B. *J. Chem. Phys.* **1995**, *102*, 3202.
(3) Morgan, C. G.; Drabbels, M.; Wodtke, A. M. *J. Chem. Phys.* **1996**, *105*, 4550.
(4) Gezelter, J. D.; Miller, W. H. *J. Chem. Phys.* **1996**, *104*, 3546.
(5) Seideman, T.; Miller, W. H. *J. Chem. Phys.* **1992**, *97*, 2499.
(6) Allen, W. D.; Schaefer, H. F., III. *J. Chem. Phys* **1988**, *89*, 329−344.
(7) Cui, Q.; Morokuma, K. *J. Chem. Phys.* **1997**, *107*, 4951−4959.
(8) Yarkony, D. R. *J. Phys. Chem. A* **1997**, *101*, 4263−4270.
(9) Yarkony, D. R. *Acc. Chem. Res.* **1998**, *31*, 511−518.
(10) Yarkony, D. R. *J. Chem. Phys.* **1999**, *110*, 701−705.
(11) Woywood, C.; Domcke, W.; Sobolewski, A.; Werner, H.-J. *J. Chem. Phys.* **1994**, *100*, 1400−1413.
(12) Trofimov, A. B.; Köppel, H.; Schirmer, J. *J. Chem. Phys.* **1998**, *109*, 1025−1040.
(13) Shavitt, I. The Method of Configuration Interaction. In *Modern Theoretical Chemistry*; Schaefer, H. F., Ed.; Plenum Press: New York, 1976; Vol. 3, p 189.
(14) Roos, B. O.; Taylor, P. R.; Siegbahn, P. E. M. *Chem. Phys.* **1980**, *48*, 157.
(15) Lengsfield, B. H.; Yarkony, D. R. Nonadiabatic Interactions Between Potential Energy Surfaces: Theory and Applications. In *State-Selected and State to State Ion−Molecule Reaction Dynamics: Part 2 Theory*; Baer, M., Ng, C.-Y., Eds.; John Wiley and Sons: New York, 1992; Vol. 82, pp 1−71.
(16) Dunning, T. H. *J. Chem. Phys.* **1971**, *55*, 716.
(17) Yarkony, D. R. Electronic Structure Aspects of Nonadiabatic Processes in Polyatomic Systems. In *Modern Electronic Structure Theory*; Yarkony, D. R., Ed.; World Scientific: Singapore, 1995; pp 642−721.
(18) Yarkony, D. R. *Rev. Mod. Phys.* **1996**, *68*, 985−1013.
(19) East, A. L. L.; Allen, W. D.; Klippenstein, S. J. *J. Chem. Phys* **1995**, *102*, 8506−8532.
(20) Huber, K. P.; Herzberg, G. *Molecular Spectra and Molecular Structure IV. Constants of Diatomic Molecules*; Van Nostrand Reinhold: New York, 1979.
(21) Klippenstein, S. J.; East, A. L. L.; Allen, W. D. *J. Chem. Phys* **1996**, *105*, 118−140.
(22) Andersson, K.; Roos, B. O. Multiconfigurational SEcond order perturbation theory. In *Modern Electronic Structure Theory*; Yarkony, D. R., Ed.; World Scientific: Singapore, 1995; Vol. 2, pp 55−109.
(23) Yarkony, D. R. Molecular Structure. In *Atomic, Molecular and Optical Physics Handbook*; Drake, G. L., Ed.; AIP: New York, 1996; pp 357−377.
(24) Kuntz, P. J.; Whitton, W. N.; Paidarova, I.; Polak, R. *Can. J. Chem.* **1994**, *72*, 939.
(25) Chaban, G.; Gordon, M. S.; Yarkony, D. R. *J. Phys. Chem. A* **1997**, *101*, 7953−7959.
(26) Glezakou, V.-A.; Gordon, M. S.; Yarkony, D. R. *J. Chem. Phys.* **1998**, *108*, 5657−5659.
(27) Sadygov, R. G.; Yarkony, D. R. *J. Chem. Phys.* **1999**, *110*, 3639−3642.
(28) Yarkony, D. R. *J. Chem. Phys.*, submitted.
(29) Yarkony, D. R. *Theor. Chem. Acc.* **1997**, *98*, 197−201.
(30) Yarkony, D. R. Diabatic potential curves and avoided crossings for diatomic molecules. In *Theoretical High Resolution Molecular Spectroscopy*; Jensen, P., Bunker, P., Eds.; John Wiley andSons: New York, 1999.
(31) Werner, H. J.; Meyer, W. *J. Chem. Phys.* **1981**, *74*, 5802−5807.
(32) Yarkony, D. R. *J. Phys. Chem. A* **1998**, *102*, 8073−8077.
(33) Macías, A.; Riera, A. *J. Phys. B.* **1978**, *11*, L489−L492.
(34) Hettema, H.; Yarkony, D. R. *J. Chem. Phys.* **1995**, *102*, 8431.
(35) Tully, J. C. *J. Chem. Phys.* **1974**, *61*, 61.
(36) Zahr, G. E.; Preston, R. K.; Miller, W. H. *J. Chem. Phys.* **1975**, *62*, 1127−1135.
(37) Köppel, H.; Domcke, W.; Cederbaum, L. S. *Adv. Chem. Phys.* **1984**, *57*, 59.
(38) Brown, S. S.; Berghout, H. L.; Crim, F. F. *J. Chem. Phys* **1995**, *102*, 8440.
(39) Brown, S. S.; Berghout, H. L.; Crim, F. F. *J. Chem. Phys.* **1995**, *102*, 8440.
(40) Matsunaga, N.; Yarkony, D. R. *J. Chem. Phys.* **1997**, *107*, 7825−7838.
(41) Matsunaga, N.; Yarkony, D. R. *Molec. Phys.* **1998**, *93*, 79−84.